PCCP

PAPER

View Article Online
View Journal | View Issue

Check for updates

Cite this: *Phys. Chem. Chem. Phys.*, 2018, **20**, 28075

How a linear triazene photoisomerizes in a volume-conserving fashion†

Alireza Marefat Khah,[a] Lena Grimmelsmann,[b] Johannes Knorr,[b] Patrick Nuernberger*[b] and Christof Hättig*[a]

Received 15th August 2018,
Accepted 24th October 2018

DOI: 10.1039/c8cp05208e

rsc.li/pccp

Understanding deactivation mechanisms of functional groups is a key step to design novel photo-active devices and molecular imaging agents. Here, we elucidate the photochemistry of linear triazenes, an extended analogue of the photo-switchable azo group, exemplarily for the widely used DNA-minor-groove binder berenil. Combining ultrafast spectroscopy and *ab initio* calculations unveils that the *E*-azo,s-*trans* structure of berenil predominates in the gas phase and in aqueous solution, and ADC(2) intrinsic reaction coordinate calculations disclose that the excited-state relaxation to the S_1 minima/conical intersections follows a two-step mechanism: N=N bond stretching followed by a bicycle-pedal rotation in the triazene bridge. Furthermore, studying the ground-state pathways shows that a fraction of the molecules relaxes back to the *E*-azo,s-*trans* isomer while the other part photoisomerizes to the *Z*-azo,s-*trans via* a hula-twist motion, as evidenced by experimental quantum yields of $\Phi \approx 0.5$ found for berenil in water, ethylene glycol, or bound to β-trypsin. Moreover, our studies show that while the excited-state relaxation is insensitive to the environment, the ground-state dynamics depend on biomolecular binding partners.

Published on 25 October 2018. Downloaded by Ruhr Universitat Bochum on 12/22/2018 1:37:31 PM.

1 Introduction

Light-induced *cis–trans* isomerizations are rather simple processes for the conversion of electronic energy into kinetic energy on a molecular scale. Despite the notation "simple", these processes are extensively studied because of the large variety of applications in biology, chemistry and technology. They are for example involved in the primary step of vision,[1,2] optical data storage devices[3,4] and switchable molecular motors.[5–7] Many photoisomerization processes occur on a (sub-)picosecond timescale. With the development of ultrafast laser sources the investigation of these phenomena in real time became feasible. From a theoretical point of view, conical intersections serve as efficient funnels from an upper to a lower electronic state. Substantial structural changes can lead excited molecules to and "through" a conical intersection and thus are often the reason for an ultrashort excited-state lifetime. Azobenzene and stilbene present two of the most extensively studied systems featuring rapid photoisomerization processes which involve a conical intersection. Despite the similarities in their molecular structure, the excited-state dynamics differ significantly. Azobenzene exhibits ultrafast excited-state dynamics even under strong constraints,[8] whereas, because of the different isomerization mechanism, for stilbene the dynamics are slowed down. For azobenzene, a hula-twist mechanism is proposed,[9] while stilbene isomerizes *via* rotation around the C=C double bond.[10] Moreover, in the literature further mechanisms are described for these and other organic chromophores which can be classified as either large-amplitude or volume-conserving motions. Inversion and rotation belong to the former class,[9] whereas the hula-twist, the NN-twist, the bicycle-pedal motion and related torsional mechanisms are characterized as volume-conserving.[11–16]

The investigation of the *cis–trans* isomerization of triazenes started in 1972 with the discovery of silyltriazenes by Wiberg and Pracht.[17,18] However, for many triazenes, photogenerated isomers are thermally unstable and reform the initial configuration so that time-resolved spectroscopy techniques are necessary to allow an observation. For this reason, initially only those triazenes forming rather stable isomers were investigated,[19] later insightful work with various spectroscopy approaches on the ground-state isomerization processes after photoexcitation was reported for 1,3-diphenyltriazene.[20–23] The triazene compound diminazene, which is of interest in the present study, is in combination with its counterion aceturate well-known as berenil, a widely used drug for treating the sleeping sickness in animals.[24] Depending on the environment, the fluorescence intensity of berenil differs significantly. While a characteristic blue fluorescence can be detected when berenil is added to cell cultures

[a] *Theoretische Chemie, Ruhr-Universität Bochum, 44780 Bochum, Germany. E-mail: christof.haettig@rub.de*
[b] *Physikalische Chemie II, Ruhr-Universität Bochum, 44780 Bochum, Germany. E-mail: patrick.nuernberger@rub.de*

† Electronic supplementary information (ESI) available. See DOI: 10.1039/c8cp05208e

Published on 25 October 2018. Downloaded by Ruhr Universitat Bochum on 12/22/2018 1:37:31 PM.

which are in the stationary or lag phase of a growth cycle, the fluorescence is absent when berenil is added to cells in the log phase.[24] The virtual absence of fluorescence is also characteristic for solutions of berenil in organic solvents,[25,26] which indicates rapid deactivation dynamics. In a recent communication,[27] the excited-state relaxation pathway of berenil was explored by means of femtosecond fluorescence upconversion spectroscopy and wavefunction-based *ab initio* calculations at the level of the algebraic diagrammatic construction through second order, ADC(2). It was found that ultrafast excited-state dynamics proceed on a sub-picosecond timescale even under strong constraints, showing similarities but also differences with regard to azobenzene.[8] This unexpected insensitivity to changes in the molecular environment and the ultrafast excited-state relaxation of the ET1 conformer (*vide infra*) were rationalized through an analysis of the intrinsic reaction coordinates (IRC). It was illustrated that the deexcitation mechanism consists of two phases: an elongation of the N=N double bond followed by a bicycle-pedal-type motion of conjugated bonds which minimizes the energy to a conical intersection between the lowest electronically excited and the ground state. This volume-conserving motion can explain the lack of sensitivity to viscous environments (as recently confirmed in high-pressure studies[28]) and the binding to large biomolecules as well as the extremely short emission lifetime. The study concentrated solely on excited-state dynamics, and the employed technique of fluorescence upconversion only allowed the pursuit of emissive reaction pathways. Following absorption changes on the femtosecond timescale would further open the possibility to observe spectral signatures associated with the formation and dynamics of ground-state species.

In the current study, the ultrafast photodynamics of berenil are investigated with transient absorption spectroscopy. This complements extensive *ab initio* MP2 and ADC(2) calculations and the analysis of the IRC pathways which are used to provide molecular insight into the involved ground- and excited-state processes. Dissecting the role of different ground-state conformers and the (photo-)isomerization pathways allows us to draw a comprehensive picture which connects the steady-state and transient absorption spectra of berenil with light-induced geometrical changes as elucidated by the calculations.

2 Material and methods

2.1 Sample preparation

Berenil, β-trypsin and ethylene glycol were purchased from Sigma Aldrich. For the experiment with trypsin, a solution of 4.5 mg berenil and 15 mL 50 mM Tris–HCl and 25 mM $CaCl_2$ was prepared. Afterwards 244.7 mg of β-trypsin were added. In the case of pure buffer, 28.8 mg berenil were dissolved in 25 mL buffer (for the UV white-light probe studies) or 10.3 mg berenil were dissolved in the same volume of buffer (for the visible white-light probe studies). For the ethylene glycol studies, 10.4 mg berenil were dissolved in 25 mL of ethylene glycol for the probe with visible white-light and 30.6 mg berenil for the probe with UV white-light, respectively. For all solutions, the final optical density of the sample, prepared in fused-silica cuvettes (Hellma) with a path length of 0.02 cm, was verified using an absorption spectrometer (Jasco V-770). The absorption was again measured after the time-resolved measurements to exclude the possibility of pronounced photodegradation.

2.2 Transient absorption

The femtosecond transient absorption (TA) setup comprises an amplified laser system (Spitfire Ace, Spectra Physics) delivering near-infrared pulses (central wavelength 800 nm, pulse energy 4.2 mJ, pulse duration 100 fs, repetition rate 1 kHz). Frequency-doubling to 400 nm in a β-barium borate (BBO) crystal yields the pump pulses employed in the TA experiments. Every second pump pulse is blocked by a chopper driven at 500 Hz. A small fraction of the 800 nm pulses are used to pump a linearly moving calcium fluoride (CaF_2) disk to generate the white-light continuum in the wavelength range between 320 and 610 nm, which serves as probe pulses. The integration of another BBO crystal in front of the CaF_2 plate and the use of adequate filters leads to a UV white-light continuum between 280 and 390 nm. Magic angle configuration is used to eliminate anisotropy effects.[29,30] Both pump and probe beams overlap in the sample solution, which is circulated through a 0.02 cm path length flow cell. The pump pulse is blocked behind the sample, whereas the white-light signal is guided to a spectrometer (Acton SpectraPro SP2500i, grating 150 grids per mm) with an attached CCD camera (Roper Scientific, binned to 1024 pixels at 1 kHz readout). A sketch of the setup is shown in the ESI.†

TA spectra were recorded at 400 time delays from −1 ps to 3.8 ns. 250 steps are equidistant from −1 to 15 ps and 150 time steps are spaced on a logarithmic time scale. At each delay, 3000 spectra were recorded and the TA spectra were calculated according to

$$\Delta A(\lambda_{\text{probe}}, t) = -\lg\left[\frac{I_{\text{pumped}}(\lambda_{\text{probe}}, t)}{I_{\text{unpumped}}(\lambda_{\text{probe}})}\right], \quad (1)$$

where $I_{\text{pumped}}(\lambda_{\text{probe}},t)$ and $I_{\text{unpumped}}(\lambda_{\text{probe}})$ represent the probe intensity in presence and absence of a pump pulse, respectively. Afterwards, the 1500 TA spectra per delay time were averaged. Altogether, at least 8 TA maps are averaged per sample. The presented TA maps are corrected for background light and for the chirp of the probe beam,[30,31] for which the temporal center of the coherent artifact is extracted and fitted with a third-order polynomial. The analysis of the TA maps is performed using the software GloTarAn[32] which also accounts for the instrument response function and the coherent artifact.

2.3 Computational methods

The *ab initio* calculations were carried out with the TURBOMOLE[33] program package. For the ground-state geometry optimizations the B3LYP-D3(bj)/def2-TZVP[34–37] functional and basis set are used. They are combined with MP2/def2-TZVP single point calculations to obtain the relative energies of the conformers. The MP2 and ADC(2) calculations used the resolution-of-the-identity approximation with the corresponding optimized

 This journal is © the Owner Societies 2018

Published on 25 October 2018. Downloaded by Ruhr Universitat Bochum on 12/22/2018 1:37:31 PM.

auxiliary basis sets[38] and the frozen-core approximation on the optimized SCF 1s core orbitals of the C, N and O atoms. The polarizable conductor-like screening model (COSMO)[39] is used to calculate the MP2 ground-state energies (COSMO-MP2) in aqueous solution (ε = 50, r_{solv} = 1.3333 Å). The solvation effects are also included in the excitation energy and transition moment calculations with PTED-COSMO-ADC(2)[40] including a perturbative correction for the state specific contribution to excitation energies (hereafter COSMO-ADC(2)) reported in Table 2 and the simulated absorption spectra shown in Fig. 2b.

The vertical excitation energies and one-photon oscillator strengths are calculated with the algebraic diagrammatic construction through second[41] order, ADC(2), a propagator method which is based on the same ground-state wavefunction as MP2. From a practical point of view, ADC(2) can also be seen as a modification[42] of the coupled-cluster method CC2,[43] which in difference to the latter has a hermitian secular matrix and uses, like MP2, a strict first-order truncation for the ground-state wavefunction. ADC(2) provides the same accuracy[44] for excitation energies as CC2, but has about four times lower computational costs for the calculation of gradients,[42] *i.e.* excited-state structure optimization and intrinsic reaction coordinate[45] (IRC) calculations.

The ground- and excited-state relaxation of the ET conformer are studied by analyzing the IRC paths calculated with MP2/SVP (ground state) and ADC(2)/SVP (excited state). The calculations have been started from the Frank–Condon (FC) point or (slightly distorted) transition state or bifurcation point (second-order saddle point) structures. The initial velocities of the atoms were set to zero. Then the molecule is moved on the Born–Oppenheimer potential energy surface (PES) with respect to the forces that are obtained from classical Newtonian mechanics with a fixed time interval. In the next step, the atomic velocities are again set to zero and the last step is repeated until the components of the Cartesian molecular gradients became smaller than a defined threshold. With a properly small time interval, this procedure allows to smoothly probe the PESs and provides a way to map the connectivity network between the stationary points. The so obtained IRC paths are used in the current work to determine relaxation and isomerization mechanisms. Furthermore, the last point of each IRC calculation was used for a numerical (or an analytical) frequency calculation at the same level of theory and as an initial structure for a transition state or a geometry optimization calculation, which is used to confirm that two stationary points are indeed connected. The reaction pathways for the conversion of the *Z*-azo,s-*trans* and *E*-azo,s-*cis* conformers into the *E*-azo,s-*trans* conformer on the ground-state PES were obtained with the chain-of-states method[46] which is implemented in woelfling program of the TURBOMOLE package. Finally, the excited-state absorption (ESA) spectra[47] and relative energies of the ground- and excited-state stationary points of the most stable conformers are calculated with ADC(2)/aug-cc-pVTZ using structures optimized, respectively, at the MP2/cc-pVTZ (ground state) and ADC(2)/cc-pVTZ (excited state) level of theory.

3 Results and discussion

3.1 Computational assessment of ground-state conformers

The computational investigation starts with searching for the most stable ground-state conformers. Starting from different initial structures of berenil, we could identify six distinct conformers, which appear as three pairs of spatial conformers of the triazene functional group as shown in Fig. 1 based on the B3LYP-D3(bj)/def2-TZVP geometry optimizations: *E*-azo,s-*trans* (ET1,ET2), *E*-azo,s-*cis* (EC1,EC2) and *Z*-azo,s-*trans* (ZT1,ZT2) pairs where 1 and 2 stand for gauge and eclipsed relative orientation of the terminal amidinium functional groups that are twisted by $\approx$30 degrees out of the molecular plane. Cartesian coordinates of all conformers are available in ESI.†

The DFT-optimized geometries were used for single point calculations with MP2/SVP and MP2/def2-TZVP. The close agreement of the energy differences between the conformers at the MP2/SVP, MP2/def2-TZVP and DFT/B3-LYP-D3(bj)/def2-TZVP levels of theory shows that this molecule is not a strongly correlated system and that the DFT optimized geometries are reliable. Therefore, the second-order treatment of the correlation energy in the MP2 and ADC(2) methods should be sufficient. Both DFT and MP2 agree on the fact that the ZT1 and ZT2 conformers have high relative energies. Furthermore, similar Boltzmann probabilities for ET1 and ET2 show that the relative orientation of the amidinium groups is not important for the energy. With a set of single point energy calculations with the SVP basis set (which has less basis functions) at the MP2 level, the basis set dependence of the relative energies of conformers is investigated. The insensitivity of the results to this change indicates that the smaller SVP basis set should be sufficient for the relaxation and isomerization pathway calculations. Finally, based on these calculations, we conclude that in vacuum and

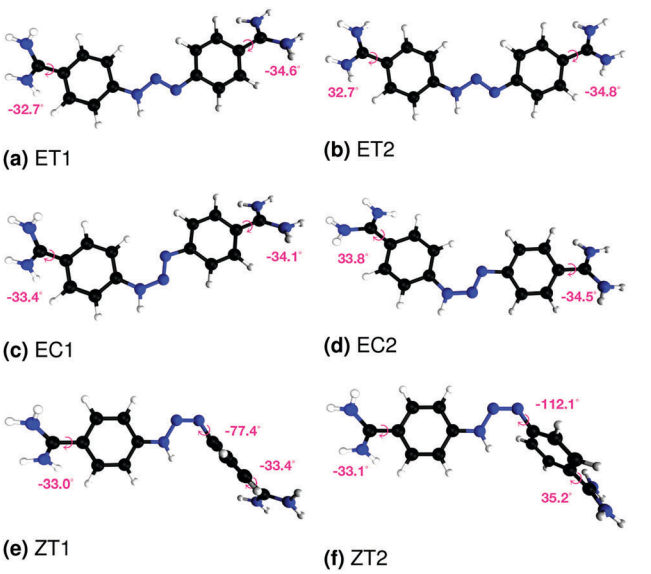


Fig. 1 The structure of berenil ground-state conformers computed at B3LYP-D3(bj)/def2-TZVP level of theory. All of the conformers are approximately planar with respect to torsion angles that are not specified.

Published on 25 October 2018. Downloaded by Ruhr Universitat Bochum on 12/22/2018 1:37:31 PM.

Table 1 The relative energies in kcal mol^{-1} and relative Boltzmann probabilities (W_B) at T = 298 K of different conformers with different methods and basis sets. Vacuum results are indicated by "VAC" and the COSMO results by "COSMO"

Conformer	Method	Basis set	ΔE	W_B
ZT1	B3-LYP(VAC)	def2-TZVP	14.3	0.00
ZT2	B3-LYP(VAC)	def2-TZVP	14.3	0.00
ET1	B3-LYP(VAC)	def2-TZVP	0.0	0.50
ET2	B3-LYP(VAC)	def2-TZVP	0.0	0.50
EC1	B3-LYP(VAC)	def2-TZVP	4.4	0.00
EC2	B3-LYP(VAC)	def2-TZVP	4.4	0.00
ZT1	MP2-VAC	def2-TZVP	14.4	0.00
ZT2	MP2-VAC	def2-TZVP	14.4	0.00
ET1	MP2-VAC	def2-TZVP	0.0	0.50
ET2	MP2-VAC	def2-TZVP	0.0	0.50
EC1	MP2-VAC	def2-TZVP	4.0	0.00
EC2	MP2-VAC	def2-TZVP	4.0	0.00
ZT1	MP2-VAC	SVP	15.6	0.00
ZT2	MP2-VAC	SVP	15.6	0.00
ET1	MP2-VAC	SVP	0.0	0.50
ET2	MP2-VAC	SVP	0.0	0.50
EC1	MP2-VAC	SVP	4.0	0.00
EC2	MP2-VAC	SVP	4.0	0.00
ZT1	COSMO-MP2	SVP	16.3	0.00
ZT2	COSMO-MP2	SVP	16.3	0.00
ET1	COSMO-MP2	SVP	0.0	0.50
ET2	COSMO-MP2	SVP	0.0	0.50
EC1	COSMO-MP2	SVP	3.3	0.00
EC2	COSMO-MP2	SVP	3.2	0.00

thermodynamically equilibrated conditions at T = 298 K, the most stable and dominantly occupied conformers of berenil are the *E*-azo,s-*trans* conformers (ET1 and ET2) with the same Boltzmann probabilities (W_B). The COSMO-MP2 results listed in Table 1 show that the ET1 and ET2 conformers stay the most stable conformers in aqueous solutions with the same probability. The relative orientation of the amidinium groups plays again no role for the ground-state energies even with inclusion of implicit solvent interactions. Also, the other conformers show this trend consistently at different levels of theory.

3.2 Simulation of steady-state absorption

The vertical excitation energies and oscillator strength for the 5 lowest electronically excited states of berenil are calculated at the COSMO-ADC(2) level with the aug-cc-pVDZ (aDZ) and SVP basis sets using the DFT-optimized ground-state geometries. The results are shown in Table 2. In general, for the most stable ground-state conformers ET1 (Fig. 1a) and ET2 (Fig. 1b), the COSMO and vacuum results are close. Furthermore, the minima of the unrelaxed torsion potentials, calculated at COSMO-ADC(2)/SVP level (available in ESI,† Fig. S1) are close to the fully optimized vacuum ADC(2)/SVP structure and thus the optimized excited-state geometries found in the vacuum calculations can be expected to be close to those that would be found with COSMO. Although in COSMO-ADC(2) calculations the vertical excitation energies of the lowest excited states of the ET conformer change by approximately 0.2 eV from the SVP to the aDZ basis set, a natural transition orbital (NTO) analysis indicates that the character of the excitation of the first two

Table 2 Electronic transitions of the ET and EC conformers calculated at the ADC(2) and COSMO-ADC(2) levels with the SVP and aDZ basis sets. Vertical excitation energies (ΔE in eV) and oscillator strengths (f) are shown

	Vacuum		COSMO			
	SVP		SVP		aDZ	
State	ΔE	f	ΔE	f	ΔE	f
$ET1_{S1}$	3.54	1.30	3.52	1.28	3.32	1.17
$ET1_{S2}$	3.73	0.01	3.87	0.00	3.84	0.00
$ET1_{S3}$	4.61	0.00	4.66	0.01	4.53	0.01
$ET1_{S4}$	4.65	0.09	4.77	0.02	4.58	0.08
$ET1_{S5}$	4.75	0.02	4.92	0.12	4.74	0.09
$ET2_{S1}$	3.54	1.30	3.52	1.27	3.32	1.17
$ET2_{S2}$	3.73	0.01	3.88	0.00	3.84	0.00
$ET2_{S3}$	4.61	0.00	4.66	0.01	—	—
$ET2_{S4}$	4.65	0.09	4.77	0.02	—	—
$ET2_{S5}$	4.75	0.02	4.92	0.11	—	—
$EC1_{S1}$	3.60	0.29	3.64	1.14	3.49	1.17
$EC1_{S2}$	3.65	0.92	3.74	0.08	3.69	0.01
$EC1_{S3}$	4.64	0.02	4.71	0.02	4.58	0.02
$EC1_{S4}$	4.73	0.04	4.78	0.00	4.64	0.01
$EC1_{S5}$	4.77	0.05	5.00	0.09	4.78	0.07
$EC2_{S1}$	3.59	0.39	3.64	1.04	3.49	1.15
$EC2_{S2}$	3.68	0.81	3.76	0.17	3.70	0.04
$EC2_{S3}$	4.65	0.02	4.71	0.02	—	—
$EC2_{S4}$	4.73	0.04	4.79	0.00	—	—
$EC2_{S5}$	4.77	0.05	5.01	0.09	—	—

excited states are similar for the SVP and aDZ basis sets (see ESI,† Tables S1–S4) and the SVP results are still accurate enough for qualitative purposes regarding the stationary points and the dynamics while the ADC(2)/aDZ calculations can reproduce the experimental results almost quantitatively. Moreover, it is seen that solvent effects have a minimal impact on both the vertical excitation energies (a 0.08 eV solvatochromic red-shift with aDZ basis set) and the oscillator strength of the lowest excited state (a bright state with N=N$_{\pi\pi^*}$ character) of the ET conformer while they cause a 0.15 eV blue-shift of the second excited state, a dark state with N=N$_{n\pi^*}$ character. The aDZ results are available in the ESI,† Tables S3 and S4. The observed solvatochromic red-shift of the bright state can be understood by the interaction between the transition density of the solute and the solvent which stabilizes excited states typically the more the larger the transition moments are. On the other hand, nπ* excitations of organic chromophores are in polar solvent usually blue-shifted because of the reduced interaction between the lone-pair (n) and the solvent in the excited state. This opposite response of ππ* and nπ* excited states can cause a switching between the states when they are close in energy and, indeed, in the case of the EC conformer, the NTO analysis of the vacuum ADC(2)/SVP results shows an N=N$_{n\pi^*}$ character for the lowest excited state while at the COSMO-ADC(2)/SVP level, the lowest excited state has N=N$_{\pi\pi^*}$ character. With the larger aDZ basis, however, the N=N$_{\pi\pi^*}$ state is already in vacuum the lowest excited state and stays the lowest in solution. The energy gaps between the first and second excited state are with the aDZ basis 0.1 eV in vacuum and 0.2 eV in aqueous solution. NTOs from the (COSMO-)ADC(2)

 This journal is © the Owner Societies 2018

Published on 25 October 2018. Downloaded by Ruhr Universitat Bochum on 12/22/2018 1:37:31 PM.

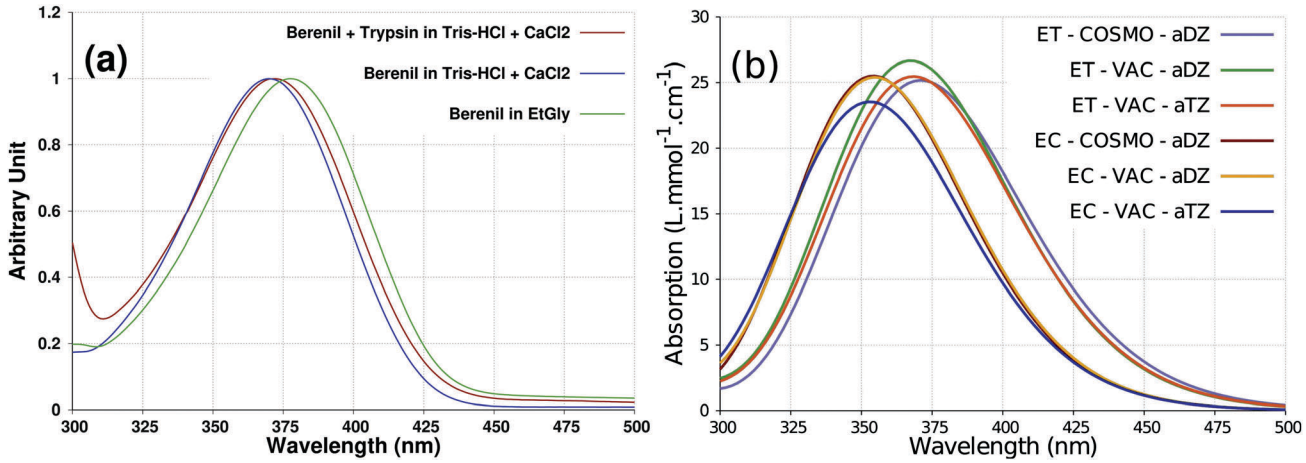


Fig. 2 (a) Normalized experimental steady-state absorption spectra of berenil in different environments. (b) Steady-state absorption spectra calculated at COSMO-ADC(2)/ and ADC(2)/aug-cc-pVXZ (X = D,T) levels with 0.3 eV broadening factor.

calculations with the SVP and aDZ basis sets are available in Tables S5–S8 of the ESI.† Because of the small energy gap between the N=N$_{\pi\pi^*}$ and N=N$_{n\pi^*}$ states one can expect relatively complex excited-state dynamics for the meta-stable EC conformer.

To further validate the stability of the results with respect to the basis-set size and to compare the theoretical and experimental spectra, the steady-state absorption spectra of berenil under different experimental conditions and the simulated spectra from COSMO-ADC(2)/aDZ, ADC(2)/aDZ and ADC(2) in the aug-cc-pVTZ (aTZ) basis are shown in Fig. 2. The experimental extinction coefficient of berenil in distilled water is reported to be $\varepsilon_{exp} = (26.5 \pm 2.3)$ mM^{-1} cm^{-1} at a wavelength of 368 nm,[48] which is very close to the theoretical values (373 and 368 nm) with the aDZ and aTZ basis sets, respectively. Also the SVP results are only shifted by 0.2 eV. Therefore, we will use the both types of basis sets to take advantage of their performance and accuracy, *i.e.* using the aug-cc-pVXZ (X = D,T) basis sets whenever a quantitative comparison with the experimental results is needed and the smaller SVP basis set for the calculation of deexcitation and reaction pathways. Moreover, the results in Table 2 reveal that the first electronically excited state has the highest oscillator strength among those that appear below 5 eV. Table 2 also shows that neither the vertical excitation energies nor the oscillator strengths change with the relative orientation of the amidinium groups for both the EC and the ET conformers. Therefore, hereafter, we will only consider the ET1, EC1 and ZT1 conformers and will omit the "1" from the abbreviated names.

The above conclusions corroborate our previously reported study[27] of the excited-state pathways of berenil where the lead conformer, ET, was analyzed to understand the measured fluorescence upconversion data and to clarify the deexcitation mechanism. Albeit our calculations predict a probability close to 0% for the conformers other than ET, we want to point out that the vertical excitation energies of the lowest singlet excitation of the ET and EC conformers are as close as $\approx$0.1 eV and therefore it would be difficult to identify putative trace amounts of the less stable conformer EC based on the steady-state absorption spectrum. Thus, in the calculations further below, we will concentrate on the most stable conformer ET, as the lead conformer of berenil, but also investigate the less stable EC and ZT conformers to examine if these conformers play a role in the photochemistry of berenil.

Due to the hydrogen atom bound to one of the nitrogens of the triazene bridge, linear triazenes have in principle the possibility of a double-bond migration by a hydrogen transfer, which could involve solvent molecules or even comprise tunneling contributions. For 1,3-diphenyltriazene, the ground-state backreaction from a *Z* to an *E* isomer proceeds significantly faster in protic solvents than in aprotic ones (ms *versus* 100 ms range), which was explained by a solvent-mediated hydrogen transfer.[20,22] We note that the ET conformers of berenil would stay the same because of the symmetry of the molecule, whereas EC and ZT could, in principle, interconvert and both conformers, ZT and EC can then isomerize to the ET structure which explains why the ET isomer is always reformed in our samples even when photoisomers are generated (see below).

3.3 Transient absorption measurements

The TA maps of berenil in different environments are displayed in Fig. 3 (left columns). At first glance, all maps look very similar and show a negative signal centered around 370 nm, a positive transient signal around 480 nm, and a weak positive signal centered at 300 nm. The most pronounced differences arise at the long-wavelength region of the maps.

A global analysis of the TA data recorded using the visible white-light was performed, yielding three time constants for the TA map of the buffer and the ethylene glycol solutions, and four time constants when berenil is bound to trypsin. The decay-associated spectra (DAS) are shown in Fig. 3 (right panels). The DAS component associated with the shortest decay time (red) of 0.36 ps for the buffer sample, 0.40 ps for bound berenil and 0.34 ps for the ethylene glycol sample shows negative features in the region between 320 nm and 420 nm and in the range

Published on 25 October 2018. Downloaded by Ruhr Universitat Bochum on 12/22/2018 1:37:31 PM.

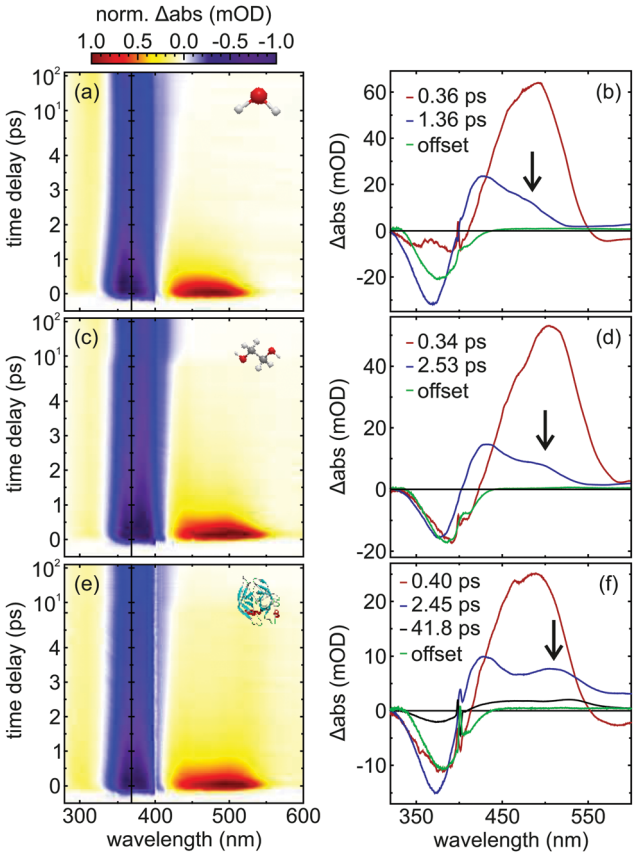


Fig. 3 Left column: Transient absorption maps for berenil pumped at 400 nm and probed in the region between 280 and 368 nm with UV white-light (narrow panel) and in the visible white-light region between 368 and 600 nm (wide panel). At 368 nm the data is normalized to −1 for comparison (see color coding). At 400 nm scattered pump light is visible. Right column: Corresponding decay associated spectra (DAS) and relaxation time scales resulting from global fitting using GloTarAn. The data is recorded for berenil in 50 mM Tris–HCl and 25 mM $CaCl_2$ aqueous buffer solution (a and b), for berenil in ethylene glycol (c and d), and for berenil bound to trypsin in 50 mM Tris–HCl and 25 mM $CaCl_2$ aqueous buffer solution (e and f). The arrows indicate the transient feature discussed in the text.

between 550 nm and 600 nm; however, this latter feature is only clearly visible for the buffer and trypsin sample but not for the ethylene glycol solution due to a general slight solvatochromic red-shift of the spectra. A large positive feature is present for all samples in the region above 410 nm. Our previous study has shown a broad fluorescence peak between 440 and 600 nm,[27] hence most of the corresponding stimulated emission (SE) signal overlaps with the positive signal, yet the negative signal above 550 nm confirms the SE contribution. The negative signal in the spectral region below 420 nm can be assigned to partial ground-state bleach (GSB) recovery, since the wavelength region matches well the absorption spectra shown in Fig. 2. The large positive signal red-shifted compared to the GSB can be assigned to excited-state absorption (ESA); we note that due to the parallel fit model of DAS, the absorption at early delay times is actually the sum of all DAS and not just represented by the red line. Thus, the first time constant describes berenil in the electronic excited state, in accordance with the average excited-state fluorescence decay time,[27] but with the difference that the overlapping of SE, GSB, and ESA does not allow an explicit decomposition of these excited-state dynamics into two sub-ps processes as in the emission studies.

The DAS offset component (green) shows a negative feature for all samples in the region between 330 and 440 nm. This component directly reveals a remaining GSB signal still observable after some ns. However, an absorption measurement right before and after the transient absorption experiment reveals no permanent change of the absorption. Therefore, the offset is not associated with the formation of a photoproduct that remains intact for infinite times, but it rather originates from a photoproduct that reforms to the reactant on a timescale of nanoseconds to seconds. The positive absorption at 300 nm observable in the UV white-light studies (narrow panels in Fig. 3a, c and e) which persists to ns delays can be assigned to this photoproduct (see Fig. S3 in ESI† for a DAS of berenil in buffer for the UV white-light study showing contributions from ESA in the first ps and the formation of the photoproduct). Since the steady-state absorption spectra reveal no permanent changes, it is likely to assume structural changes like a *cis–trans* photoisomerization. Our previous combined theoretical and experimental study already implied the bicycle-pedal motion as isomerization mechanism,[27] thus a different isomer can lead to the product absorption at 300 nm. The quantum yield for this photoisomerization is determined to be Φ = 0.48 for the buffer sample, Φ = 0.46 for the ethylene glycol sample and Φ = 0.47 when berenil is bound to trypsin. This is in good agreement with the quantum yield of Φ = 0.47 reported for the *E–Z* photoisomerization with respect to the N=N bond of 1,3-diphenyltriazene in methanol,[22] a system for which also the thermal ground-state backrelaxation was measured and occurs in the ms regime.[20,22] The *Z* isomer of 1,3-diphenyltriazene absorbs blue-shifted relative to the *E* form which is predominant in solution,[21] and generally the photogenerated *Z* isomers of triazenes exhibit an absorption peak at shorter wavelengths compared to the *E* isomers.[19] Hence, our data shows that a new isomer is formed after photoexcitation, and the existing literature supports the assumption of a *Z* isomer absorbing around 300 nm. As will be shown further below, the structure of the photogenerated isomer is elucidated in the quantum-chemical calculations.

The DAS components associated with the second time constant (blue) exhibit a derivative-like shape, with negative features below 400 nm and positive features above 400 nm. However, a significant difference is observable in the region around 500 nm, as indicated by arrows in Fig. 3. For berenil dissolved in buffer, a tiny shoulder around 485 nm appears. In the ethylene glycol solution the shoulder gets more pronounced and shifts to 500 nm. When berenil is bound to trypsin, a peak is clearly visible at 510 nm. Furthermore, the ratio of the positive and negative areas yields 1.4 for the buffer sample and 2 for the ethylene glycol and trypsin sample, indicating the emergence of a new peak. The associated time constants increase from 1.36 ps for the buffer sample, to 2.45 ps when bound to trypsin and 2.53 ps when dissolved in ethylene glycol. The derivative-like shape is typical for the description of a

 This journal is © the Owner Societies 2018

Published on 25 October 2018. Downloaded by Ruhr Universitat Bochum on 12/22/2018 1:37:31 PM.

shift[49,50] due to solvation and/or cooling processes.[51–53] The typical solvation time of water is on the order of 1 ps,[54] which would approximately match with τ_2^{buffer}, however the solvation time for the highly viscous solvent ethylene glycol is 30 times higher.[55,56] Therefore, solvation is likely not the process giving rise to τ_2. Cooling processes are mainly observable in systems with fast excited-state dynamics,[57] because in this case most of the excitation energy is not released by a radiative process. Instead, the energy remains in the molecule and has to be removed by vibrational cooling. The ultrafast excited-state dynamics observed for berenil hint to internal conversion leading to the population of highly excited vibrational states of the electronic ground state. This vibrational excess energy results in a red-shift of the ground-state absorption and a shifting to shorter wavelength with increasing delay time.[57–61] Since water has a larger number of low-frequency modes,[62] it can accept the excess energy more efficiently than ethylene glycol,[63] reflected in a prolongation of τ_2^{EtGly}. Hence, τ_2 is assigned to hot ground-state absorption, with $\tau_2^{trypsin}$ showing a value close to τ_2^{EtGly} implying cooling as fast as in ethylene glycol.

The assignment of the new peak at 500 nm allows various interpretations that will be discussed in the following. The red-shift in comparison to the ground-state absorption indicates an increase of the π-system of berenil. The deprotonation of the triazene bridge would lead to such an increased π-system, as is corroborated by the shifting of the absorption peak of berenil dissolved in NaOH buffer (pH 13.5) to 425 nm (see Fig. S5 in ESI†). In order to exclude that the deprotonation occurs at the amidinium groups, we performed test measurements with another triazene with different terminal groups (thiazole yellow, see ESI† for the molecular structure and Fig. S5 for the data) dissolved in water and in basic solution, which exhibit the same behavior implying that strong basic media lead to the deprotonation of the triazene bridge. Despite the well-matching spectral regions for the absorption of deprotonated berenil and the new transient peak indicated by the arrows in Fig. 3, the latter can barely be explained by deprotonation, because the time scale of 2.5 ps seems too fast for a deprotonation and subsequent reprotonation, also when considering diffusion of a released proton.[64] In a former study of 1,3-diphenyltriazene, the formation of cyclic dimers is proposed[20] which might lead to a red-shifted absorption signal in comparison to the monomer. However, the observed feature is most pronounced when berenil is bound to trypsin, where dimer formation would be sterically hindered. Another possibility is that the feature originates from a different isomer of berenil absorbing red-shifted in comparison to the ET isomer. We tend to discard this scenario, because the calculations of Section 3.1 have disclosed that only the ET isomer is stable at room temperature, and our sample volume is exchanged continuously so that also no photoproducts can accumulate. Regarding the ratio of positive and negative areas of the DAS exhibiting the peak around 500 nm, the relative increase from 1.4 (in buffer) to 2 (bound to trypsin) might indicate that the new peak is not related to the hot ground-state absorption (which then would look similar in all cases) but rather an additional process occurring on the same time scale. The fluorescence upconversion study[27] has shown that there is an emissive contribution with 1.4 ps in the case of berenil bound to trypsin, so at least some population survives for more than 1 ps in the ES. Since the peak is more pronounced for more restricted environments, it seems to be likely that a deactivating motion of berenil is hindered, as might also be reflected in the DAS associated with τ_3 only found for trypsin. The calculations hint towards a further possible origin related to distorted ground-state structures transiently present during the relaxation process (see Discussion in Section 3.5).

In the case of trypsin, the global fitting leads to this third DAS contribution (black component in Fig. 3f) with a lifetime of 41.8 ps, revealing also a derivative-like shape with a negative feature in the region between 330 and 400 nm and a positive feature for wavelengths larger than 400 nm. This positive feature is characterized by an additional peak at 525 nm. For strong solute–solvent interactions *via* hydrogen bonding, biexponential cooling dynamics are expected, because of the local heating of the first solvation shell.[65] The large binding constant (59.6×10^4 M)[66] points towards a strong interaction between berenil and trypsin, suggesting a release of the excess energy in two different ways: in addition to the fast component of 2.45 ps, the slower component of 41.8 ps might reflect how the strongly-bound trypsin, which also gets some of the excess energy, cools and thereby influences the berenil absorption features. This slowed-down cooling of berenil bound to trypsin could further be connected to the restricted volume available for the solvent molecules in the pocket where berenil binds.

Whereas the possibility of double-bond migration by hydrogen transfer in the ground state was discussed in Section 3.2, we also want to mention the scenario of an excited-state intramolecular hydrogen transfer (ESIHT), which (*e.g.* for keto–enol tautomerism) occurs on a timescale of 100 fs or even faster.[67–73] In this respect, the calculations of the ground-state conformers tells us that only the ET conformers are initially excited, which upon ESIHT would again yield ET isomers. That is, even if there was an extremely fast initial ESIHT contribution, the observed formation of a photoproduct must originate from another molecular motion, as substantiated by calculations in the following.

3.4 Deexcitations, from the excited state to the ground state

Fig. 4a shows the IRC pathways for the deexcitation after vertical excitation of the ET conformers (IRC_1–IRC_5) from the FC point *via* a transition state (ET_{TSS1}) to the minima ET_{S1} and ET_{RS1} and after deexcitation to the S_0 electronic state back to the ET ground-state equilibrium structure. The last point of each of these IRC calculations is used for a numerical frequency calculation at the same level of theory and for a transition state or geometry optimization calculation, which is used to confirm that the two stationary points are indeed connected. From Fig. 4a, it is apparent that in the first phase of the deexcitation process the N═N azo-bond is stretched which leads to a planar transition state, ET_{TSS1}. In the second phase of the deexcitation, the N═N double bond is rotated by ±90° which brings the structure close to a conical intersection between S_0 and S_1. In the earlier stage of the second phase of the S_1 state deexcitation,

Published on 25 October 2018. Downloaded by Ruhr Universitat Bochum on 12/22/2018 1:37:31 PM.

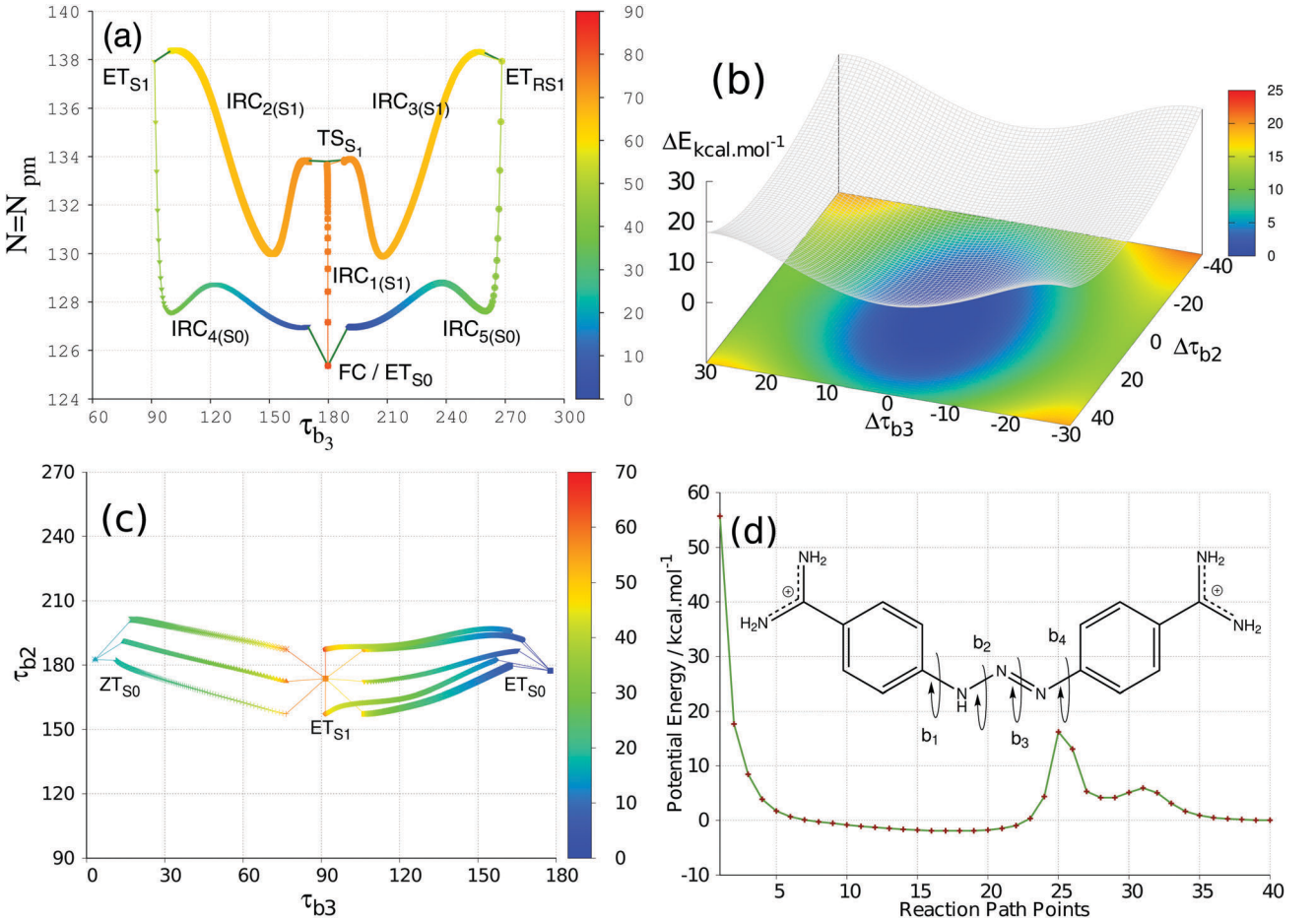


Fig. 4 (a) Evaluation of the N=N bond length and the C–N=N–N torsion angle (τ_{b3}) along the IRC_1, IRC_2 and IRC_3 paths calculated at ADC(2)/SVP level at the lowest electronically excited state and the IRC_4 and IRC_5 ground-state paths calculated at MP2/SVP level of theory. (b) Interpolated unrelaxed 2D torsion potential in the vicinity of the ET lowest electronically excited-state minimum, ET_{S1} calculated at COSMO-ADC(2)/SVP level. (c) Evaluation of the τ_{b2} and τ_{b3} torsion angles along the MP2/SVP IRC paths at the ground state starting from the screwed (±15° around τ_{b2} and τ_{b3}) ET_{S1} geometry. (d) MP2/SVP optimized reaction path starting from the ET_{S1} to EC_{S0} with 40 points and the contracted names for different torsion angles.

IRC_2 and IRC_3 in Fig. 4a, the N=N bond length decreases from 134 pm to 130 pm since the N=N bond rotation diminishes the N=N π-antibonding interaction. In the next stage of the process, the N=N bond elongates to compensate the steric and Coulomb interactions between two positively charged amidinophenyl units. The clockwise and anti-clockwise rotation around the N=N bond is energetically almost degenerate. They differ from each other's mirror image only in the torsion angles of the amidinium groups. Further details are given in the ESI.† The proposed two-phase deexcitation mechanism is confirmed by the reported fluorescence upconversion measurements.[27] The ultrafast non-radiative deexcitation of the molecule can be explained by the possibility that the molecule is funneled to the ground state *via* a conical intersection between S_0 and S_1 in a non-radiative process. Monitoring the central torsion angles along the IRC_3 trajectory, Fig. 5a reveals that the second phase of the deexcitation mechanism follows a bicycle-pedal type motion, which is a volume-conserving deexcitation path and, thus, the ultrafast deexcitation of berenil even in viscous and mechanically confined environments can be understood. The ground-state structures of the ET and ZT conformers (ET_{S0} and ZT_{S0}) and the structure of the lowest excited state minimum ET_{S1} are compared in Fig. 6. For further details about the two-phase deexcitation process and the definition of different relevant deexcitation mechanisms we refer to ref. 27.

To investigate the ground-state isomerization processes, IRC calculations (MP2/SVP) are pursued from the ET_{S1} and ET_{RS1} geometries on the ground-state PES. Both paths end in the ET_{S0} minimum, which shows that the excited molecules can be deexcited to the ground-state minimum without isomerization, IRC_4 and IRC_5 in Fig. 4a. In the ET region the relaxation on the S_1 PES funnels molecules through a conical intersection radiationless to the ground state. On the S_0 PES the relaxation proceeds through a two-step relaxation mechanism: an initial N=N bond contraction (IRC_4 and IRC_5 in Fig. 4a) which reduces the potential energy substantially and a bicycle-pedal type motion to the ET_{S0} minimum, Table 3.

However, triazene is a flexible functional group and the deexcitation does not necessarily happen at the S_1 minima or minima of the intersection seam. To examine the flexibility of

 This journal is © the Owner Societies 2018

Published on 25 October 2018. Downloaded by Ruhr Universitat Bochum on 12/22/2018 1:37:31 PM.

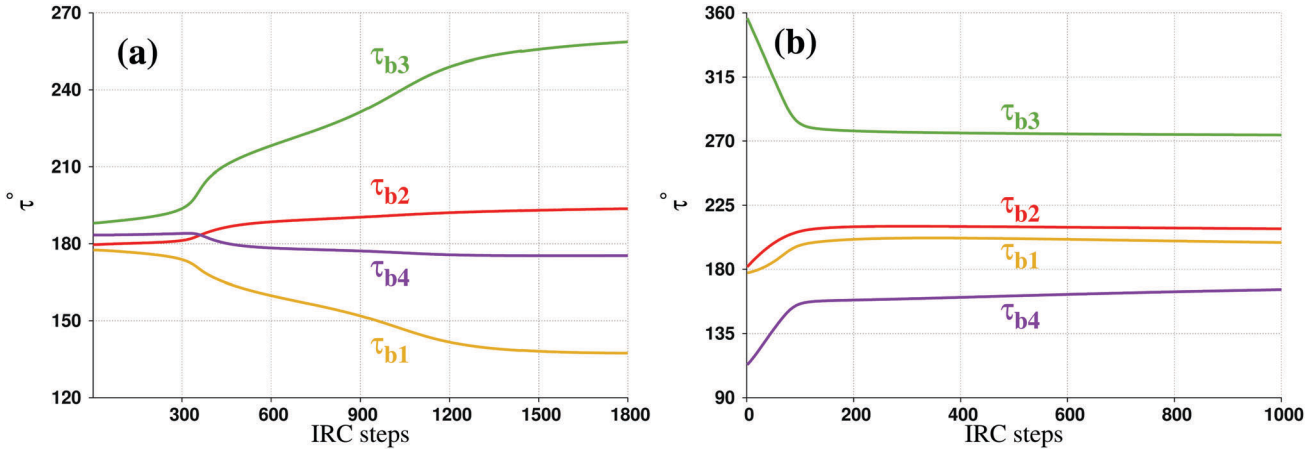


Fig. 5 Evaluations of (a) the ET conformer's triazene torsion angles along the $IRC_{3(S1)}$ path calculated at ADC(2)/SVP level (b) the ZT conformer's torsion angles along the S_1 deexcitation IRC pathway calculated at ADC(2)/SVP level, starting from the Frank–Condon point, ZT1 geometry in Fig. 1e. Geometry optimizations, starting from the final structure of both IRC paths, (a) and (b), are converged to the same minimum on the S_1 excited state, ET_{RS1}.

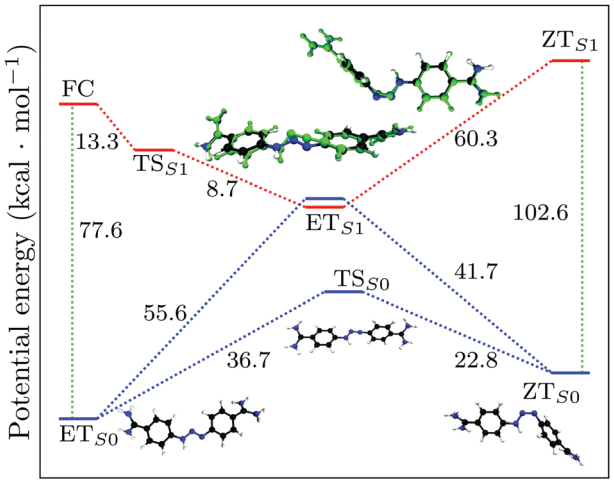


Fig. 6 Ground-state and excited-state isomerization paths of ET to ZT calculated at ADC(2)/cc-pVTZ/aug-cc-pVTZ level of theory. Color codes: (solid line) stationary and Frank–Condon point, (dotted line) geometrical changes, (blue) electronic ground-state PES, (red) lowest electronic excited state, (green) bright electronic transitions. The ground state geometries of ET and ZT conformers (atoms colors) are superimposed to the geometry of the lowest excited-state minimum, ET_{S1} (green).

Table 3 The classifications of deexcitation mechanisms are based on the maximum changes of the triazene torsion angles along the ground- and excited-state IRC pathways of the ET and ZT isomers. The Hula-twist and bicycle-pedal type mechanisms are shown with HT and BP, respectively

Transition	$\Delta\tau_{b1}$	$\Delta\tau_{b2}$	$\Delta\tau_{b3}$	$\Delta\tau_{b4}$	Mechanism
ET_{TSS1}–ET_{S1}	40.53	13.66	70.51	10.77	BP
ET_{S1}–ET_{S0}	56.80	16.55	78.03	6.13	BP
ET_{S1}–ZT_{S0}	19.58	28.04	74.27	38.42	HT
ZT_{S1}–ET_{S1}	24.56	28.55	81.92	67.21	HT

the molecule on the excited-state PES, the unrelaxed torsion potentials of τ_{b2} and τ_{b3} calculated at COSMO-ADC(2)/SVP level are interpolated with a polynomial for developing a minimal additive forcefield (see Table S9 in ESI†) to construct a two-dimensional PES around the ET_{S1} geometry as a function of τ_{b2} and τ_{b3}, Fig. 4b. The latter shows that the ET_{S1} structure is flexible enough to tolerate up to 15 degrees rotation around the τ_{b2} and τ_{b3} torsion angles. Based on this result, 8 MP2/SVP IRC calculations are run with $\pm15^\circ$ distorted ET_{S1} geometries for 500 steps, followed by MP2/SVP geometry optimizations. Fig. 4c shows the τ_{b2} and τ_{b3} torsion angles along these 8 IRC paths. It is shown that, in addition to the deexcitation path to the ET_{S0} ground-state geometry, photoisomerization to ZT_{S0} is also possible. Results in Table 3 show that on the ground-state surface, the relaxation path from ET_{S1} to ET_{S0} follows a bicycle-pedal type motion while the isomerization path to ZT_{S0} involves a hula-twist motion.

The calculated wavelength for the vertical excitation of the ZT isomer (318 nm) agrees reasonably with the experimental positive product signal of the TA maps at $\approx$300 nm. If the ZT isomer is excited from the ground state to the S_1 state, it relaxes on the S_1 surface from the Franck–Condon (FC) point to the same S_1 minima as reached when the ET isomer is excited. The deexcitation consists of a N=N bond stretch and a hula-twist[74] motion as shown in Fig. 5b (note the changes of τ_{b3} and τ_{b4}). The missing (pseudo-) planar symmetry in the case of ZT in comparison to ET and EC is the reason for the different deexcitation mechanisms. Therefore, the IRC calculation starting from the Franck–Condon point leads to the S_1 minimum without meeting a transition state located between rotatory and disrotatory twisted S_1 minima. In Fig. 6 a schematic PES of the ET and ZT isomers and their thermal and photochemical isomerization pathways are given. Cartesian coordinates are available in ESI.† It is shown that following the photoisomerization of ET to ZT, ZT can isomerize to ET on the ground state *via* a transition state and an in-plane N=N bond inversion mechanism. Note that in addition to this mechanism, solvent-mediated double-bond migration might also contribute in the ET reformation in the ground state (Section 3.2).

As discussed above, the ET conformer can be deexcited to the ZT conformer *via* the S_1 minima. But none of the IRC paths

Published on 25 October 2018. Downloaded by Ruhr Universitat Bochum on 12/22/2018 1:37:31 PM.

that are started from the screwed ET_{S1} structures, Fig. 4c, lead to the EC conformer, which is the second most stable ground-state conformer. In order to find the minimum energy path between the ET_{S1} structure and the EC_{S0} ground-state conformer, a chain-of-state method[75] is used to optimize the reaction path with 40 intermediate structures at the MP2/SVP level of theory. The potential energy along the minimum reaction path is sketched in Fig. 4d relative to the energy of the EC_{S0} minimum. This photoisomerization minimum energy path, from the ET_{S1} structure to EC_{S0}, shows that the molecule has to get first to the ET_{S0} geometry and afterwards overcome the ET-to-EC ground-state isomerization barrier to reach the EC_{S0} minimum. Based on the latter analysis and the IRC calculations of the screwed geometries, we do not expect any signal in the TA spectra from a photoisomerization process of ET to EC.

The photoisomerization mechanism of the meta-stable EC conformer (as a possible isomerization product of hot ground state ET conversion) is investigated with several excited-state geometry optimizations starting from the Franck–Condon point and geometries with the N=N torsion angle twisted by $\pm5^\circ$ on the S_1 surface at the ADC(2)/aDZ level of theory, Fig. 7. These excited-state geometry optimizations lead to two minima on the S_1 PES that cross the ground-state PES in a region close to a conical intersection. In contrast to the deexcitation processes of the ET and ZT conformers, the deexcitation processes of the EC conformer are found to be non-volume conserving. The geometries of the EC_{S0} and the minima of the excited state (EC_{S1} and EC_{RS1}) are compared in Fig. 7. Ground-state geometry optimizations that are started from EC_{S1} and EC_{RS1} and in addition from geometries with the N=N torsion angle twisted by $\pm5^\circ$ converge to the ground-state geometry of the EC conformer and two highly unstable ZC_{S0} and ZC_{RS0} conformers. However, the vertical excitation energies to the bright $\pi\pi^*$ and the dark $n\pi^*$ are for the EC conformer as close as 0.1 eV, cmp. Fig. 7, which is in the same energy regime as the solvatochromic shifts and thermal excess energies and, thus, it is expected that the EC conformer features a more complex deexcitation process rather than the experimentally observed two-step mechanism. Moreover, the vertical excitation energy of the EC conformer, neither in vacuum (3.5 eV at ADC(2)/aDZ level) nor in solvent (3.49 eV at COSMO-ADC(2)/aDZ level) match with positive signals of the TA spectra. It thus seems that the EC conformer plays no significant role for the photochemistry of berenil under the investigated conditions.

3.5 Assessing excited-state and hot ground-state absorption

The deexcitation processes explained above can be compared to the DAS of the TA studies. Based on the preceding discussion, for a qualitative description of the main spectroscopic features, considering only the dynamics of the most stable conformer ET should be sufficient. The first DAS signal (red curves in Fig. 3b, d and f) in all environments comprises strong positive absorption changes assign to excited-state absorption, ESA, exhibiting a maximum around 500 nm and possibly a shoulder around 460 nm which vanishes on the timescale of 0.4 ps. These dynamics reflect only the deexcitation process occurring in the excited state, *i.e.* the N=N bond stretching of the ET conformer and the bicycle-pedal type rotating around the τ_{b1} and τ_{b3} bonds. Both phases are, because of the reasons discussed above, expected to be associated with short relaxation time scales.

In Table 4, the vertical excitation energies and oscillator strengths for transition from the lowest excited state (S_1) to the three higher-lying singlet excited states, calculated at the ADC(2)/aTZ level using the geometries optimized at the ADC(2)/cc-pVTZ level, are listed. Based on the calculations, the TS_{S1} has a large oscillator strength for a vertical transition to the S_4 state at 459 nm which fits to the observed ESA signal. A further contribution to the ESA might be the S_1 to S_4 excitation from the second stationary point of the deexcitation pathway (ET_{S1}) occurring at 374 nm. It is worth noting that the ground-state vertical excitation from ET_{S0} to the FC point of the first

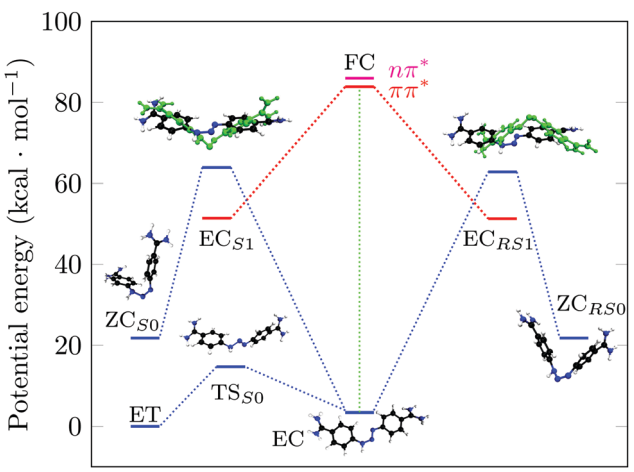


Fig. 7 Schematic potential energy surface of the gound and lowest excited states of the EC conformer calculated at ADC(2)/aug-cc-pVDZ level of theory. For color codes see the caption of Fig. 6.

Table 4 Vertical excited-state absorptions of the ET_{S1} structures. Vertical excitation energies (VEEs) and oscillator strengths (OSs) from S_1 to higher singlet ESs, calculated at ADC(2)/aTZ level at the critical points of the $ET1_{S1}$ PES, optimized at ADC(2)/cc-pVTZ level. VEEs are given in eV (nm) format

State	VEE	OS
FC		
$S_1 \rightarrow S_2$	0.39 (3179)	0.00
$S_1 \rightarrow S_3$	1.06 (1159)	0.25
$S_1 \rightarrow S_4$	1.08 (1148)	0.13
TS_{S1}		
$S_1 \rightarrow S_2$	1.83 (677)	0.00
$S_1 \rightarrow S_3$	2.09 (593)	0.02
$S_1 \rightarrow S_4$	2.70 (459)	0.87
ET_{S1}		
$S_1 \rightarrow S_2$	2.73 (454)	0.00
$S_1 \rightarrow S_3$	3.21 (386)	0.04
$S_1 \rightarrow S_4$	3.31 (374)	0.31
$S_0 \rightarrow S_1$	CI	—
$S_0 \rightarrow S_2$	2.50 (496)	0.50
$S_0 \rightarrow S_3$	2.99 (415)	0.01
$S_0 \rightarrow S_4$	3.09 (401)	0.02

This journal is © the Owner Societies 2018

Published on 25 October 2018. Downloaded by Ruhr Universitat Bochum on 12/22/2018 1:37:31 PM.

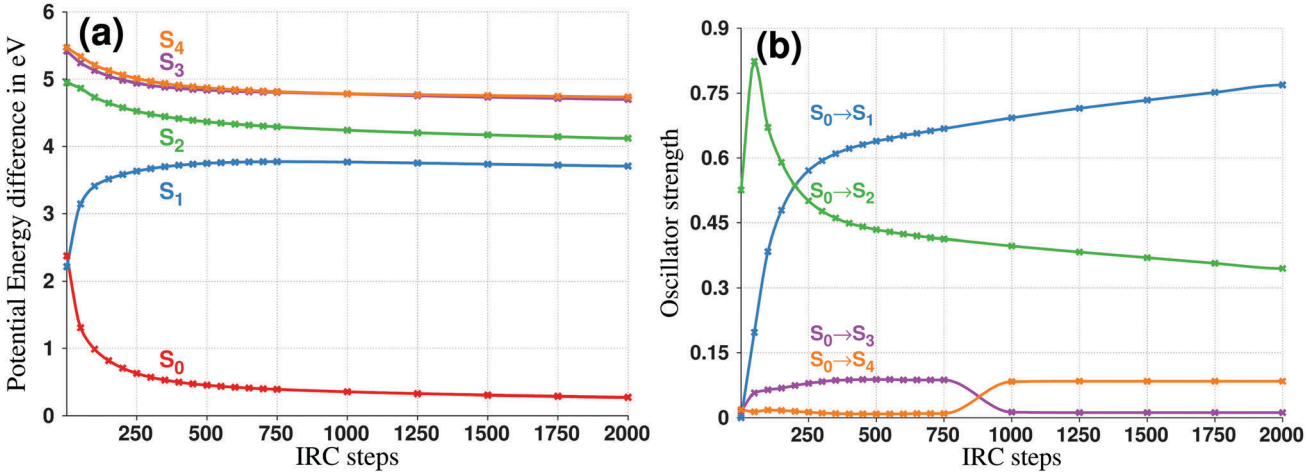


Fig. 8 (a) ADC(2)/aTZ energies of the S_0–S_4 states along the IRC_5 (Fig. 4a) pathway in eV. (b) Evaluation of oscillator strengths for excitations from ground state (S_0) to higher singlet ESs of the IRC_5 pathway calculated at ADC(2)/aTZ level. The calculations are performed for 50-step intervals up to step 750 and 250-step intervals up to step 2000 of the IRC path.

excited state (S_1) is also around 370 nm, thus in this spectral region the calculated ESA signal might overlap with the GSB contributions. In the vicinity of the ET_{S1}, molecular population of the S_1 excited state can be transferred to the ground state *via* the conical intersection. Unlike the ground-state minimum, the ET_{S1} geometry is not planar, therefore, it is possible that electronic transitions that have very low oscillator strength in the steady-state absorption (by reason of symmetry) exhibit higher oscillator strength in the transient absorption. The vertical excitation energies and oscillator strengths of excitation from the S_0 state to the 4 lowest singlet ESs at the ET_{S1} geometry (optimized at ADC(2)/cc-pVTZ level) are calculated with ADC(2)/aTZ, Table 4. At this geometry, the S_0 to S_2 is a bright excitation with a 496 nm excitation energy. The ground-state relaxation process continues on the ground-state PES with a two-step-like relaxation mechanism that is discussed in the previous section (Fig. 4a, IRC_4 and IRC_5). Fig. 8 shows the evaluation of vertical excitation energy and oscillator strength of the ground-state relaxation process along the IRC_5 path calculated at ADC(2)/aTZ level. The latter calculations and NTO analysis show that two bright excitations are involved in the ground-state relaxation process, the $S_0 \rightarrow S_1$ with a $\pi\pi^*$ character which is the dominant steady-state absorption signal and the $S_0 \rightarrow S_2$ with an $n\pi^*$ character which is transiently bright at the earlier stage of the ground-state relaxation process (blue and green curves in Fig. 8b, respectively). NTOs are given in Tables S10–S17 in ESI.† The ground-state relaxation process reestablishes the (pseudo-)planar structure of the ET_{S1} conformer which causes the decline in the oscillator strength of the $n\pi^*$ excitation and the increase in the oscillator strength of the $\pi\pi^*$ excitations due to symmetry reasons while the excitation energies only change moderately, Fig. 8a. Based on these calculations, it is expected that in the transient absorption spectra, a signal with a lifetime close to the ET_{S1} excited-state absorption peak (the 400 nm maximum of the second component of DAS spectra) appears around 496 nm (the 510 nm maximum of the second DAS component in Fig. 3f) due to the induced oscillator strength of the $n\pi^*$ excitation caused by the molecular distortion on the ground state. While the molecule relaxes to its ground state (pseudo-) planar geometry, the oscillator strength of the $S_0 \rightarrow S_2$ excitation and the energy gap of S_1 and S_2 decrease, which enhance the $S_0 \rightarrow S_1$ and $S_0 \rightarrow S_2$ signals overlap. Therefore, there is no contribution from $S_0 \rightarrow S_2$ transient absorption at longer times and the steady-state absorption has only one peak. Moreover, for the more viscous solvents or confined environments, a stronger $S_0 \rightarrow S_2$ transient absorption signal is reasonable due to the slower ground-state relaxation process, which is consistent with the experimental observation (indicated by arrows in Fig. 3b, d and f).

Based on the above discussion, either the second DAS component is caused by a contribution from the molecules that are still in the excited state and exhibit an ESA around 375 nm or the geometrically induced $S_0 \rightarrow S_2$ hot ground-state absorption with a signal at 496 nm, or both. Note that the DAS signals result from a global fit of the TA data and especially the early time dynamics must be thought of as a sum of the DAS, thereby not representing isolated but basically all participating species. Therefore, for a quantitative comparison between the computational result and the experimental data, one would have to simulate the whole dynamic processes and, for example, consider the hydrogen-transfer process as well. Nevertheless, the static approach, that is used here, is useful for acquiring a qualitative insight into the deexcitation process.

4 Conclusions

In this joint experimental and computational study of the deexcitation dynamics of the triazene compound berenil in three different environments, it could be shown that the main spectroscopic features and deexcitation mechanisms are related to the excited-state (N=N stretching, bicycle pedal motion)

Published on 25 October 2018. Downloaded by Ruhr Universitat Bochum on 12/22/2018 1:37:31 PM.

dynamics of the ET conformer occurring on a sub-ps time scale. By funneling through a conical intersection, the molecules return to the ground-state PES where one half of them reform the ET isomer and the other half isomerizes to the ZT isomer, which absorbs blue-shifted with regard to the ET isomer. Furthermore, IRC calculations of various relaxation pathways from the ET_{S1} region to the ground state and the reaction path optimization confirms that there is no barrier-less minimum energy photoisomerization pathway from the ET conformer to the EC conformer, although on the ground state there is a thermal isomerization pathway between ET and EC conformers. Through analysis of the transient absorption spectra and the calculations, a connection between experimental excited-state absorption signals and calculated absorption signatures of the transition state and the minimum of the S_1 state as well as of the geometrically induced $S_0 \rightarrow S_2$ transition, which is environment-dependent and is more pronounced in the case of berenil bound to trypsin, could be made. It is worth noting that other processes, *e.g.* ground- and excited-state proton transfers and solvent- and protein-induced relaxation can happen on the same timescale, and thus compete with the discussed mechanisms and require additional efforts to be included in the follow-up simulations. The calculations have further unveiled that other conformers of berenil, although not present in the studied solutions, exhibit a rich photochemistry. Future studies might aim at (photo)-generating these conformers and then verify whether these new reaction channels are pursued.

Conflicts of interest

There are no conflicts to declare.

Acknowledgements

This work has been supported by the Deutsche Forschungsgemeinschaft within the Cluster of Excellence RESOLV (EXC 1069).

References

1 R. W. Schoenlein, L. A. Peteanu, R. A. Mathies and C. V. Shank, *Science*, 1991, **254**, 412–415.
2 Q. Wang, R. W. Schoenlein, L. A. Peteanu, R. A. Mathies and C. V. Shank, *Science*, 1994, **266**, 422–424.
3 Z. F. Liu, K. Hashimoto and A. Fujishima, *Nature*, 1990, **347**, 658–660.
4 T. Ikeda and O. Tsutsumi, *Science*, 1995, **268**, 1873–1875.
5 N. Koumura, R. W. Zijlstra, R. A. van Delden, N. Harada and B. L. Feringa, *Nature*, 1999, **401**, 152–155.
6 C. A. Schalley, K. Beizai and F. Vögtle, *Acc. Chem. Res.*, 2001, **34**, 465–476.
7 B. L. Feringa, *Acc. Chem. Res.*, 2001, **34**, 504–513.
8 F. Renth, J. Bahrenburg and F. Temps, in *Photon-Working Switches*, ed. Y. Yokoyama and K. Nakatani, Springer, Japan, Tokyo, 2017, pp. 237–259.
9 M. Quick, A. L. Dobryakov, M. Gerecke, C. Richter, F. Berndt, I. N. Ioffe, A. A. Granovsky, R. Mahrwald, N. P. Ernsting and S. A. Kovalenko, *J. Phys. Chem.*, 2014, **118**, 8756–8771.
10 G. R. Fleming, S. H. Courtney and M. W. Balk, *J. Stat. Phys.*, 1986, **42**, 83–104.
11 M. Böckmann, N. L. Doltsinis and D. Marx, *J. Chem. Phys.*, 2012, **137**, 22A505.
12 M. Böckmann, S. Braun, N. L. Doltsinis and D. Marx, *J. Chem. Phys.*, 2013, **139**, 084108.
13 I. Schapiro, O. Weingart and V. Buss, *J. Am. Chem. Soc.*, 2009, **131**, 16–17.
14 A. Warshel, *Nature*, 1976, **260**, 679–683.
15 D. Polli, P. Altoè, O. Weingart, K. M. Spillane, C. Manzoni, D. Brida, G. Tomasello, G. Orlandi, P. Kukura, R. A. Mathies, M. Garavelli and G. Cerullo, *Nature*, 2010, **467**, 440–443.
16 J. Conyard, I. A. Heisler, Y. Chan, P. C. Bulman Page, S. R. Meech and L. Blancafort, *Chem. Sci.*, 2018, **9**, 1803–1812.
17 N. Wiberg and H. J. Pracht, *Chem. Ber.*, 1972, **105**, 1377–1387.
18 N. Wiberg and H. J. Pracht, *Chem. Ber.*, 1972, **105**, 1392–1398.
19 D. Fanghänel, G. Timpe and V. Orthman, in *Organic Photochromes*, ed. A. V. El'tsov, Consultants Bureau (Division of Plenum Publishing Corp.), New York, 1990, pp. 136–153.
20 J. Baro, D. Dudek, K. Luther and J. Troe, *Ber. Bunsenges. Phys. Chem.*, 1983, **87**, 1155–1161.
21 J. Baro, D. Dudek, K. Luther and J. Troe, *Ber. Bunsenges. Phys. Chem.*, 1983, **87**, 1161–1164.
22 J. C. Scaiano, C. Chen and P. McGarry, *J. Photochem. Photobiol., A*, 1991, **62**, 75–81.
23 M. Barra and N. Chen, *J. Org. Chem.*, 2000, **65**, 5739–5744.
24 B. A. Newton, in *Antibiotics III – Mechanism of Action of Antimicrobial and Antitumor Agents*, ed. J. W. Corcoran, F. E. Hahn, J. F. Snell, and K. L. Arora, Springer, Heidelberg Berlin, 1975, pp. 34–47.
25 D. S. Pilch, M. A. Kirolos, X. Liu, E. Plum and K. J. Breslauer, *Biochemistry*, 1995, **34**, 9962–9976.
26 V. Gabelica, F. Rosu, E. D. Pauw, R. Antoine, T. Tabarin, M. Broyer and P. Dugourd, *J. Am. Soc. Mass Spectrom*, 2007, **18**, 1990–2000.
27 L. Grimmelsmann, A. Marefat Khah, C. Spies, C. Hättig and P. Nuernberger, *J. Phys. Chem. Lett.*, 2017, **8**, 1986–1992.
28 L. Grimmelsmann, V. Schuabb, B. Tekin, R. Winter and P. Nuernberger, *Phys. Chem. Chem. Phys.*, 2018, **20**, 18169–18175.
29 S. Schott, A. Steinbacher, J. Buback, P. Nuernberger and T. Brixner, *J. Phys. B: At., Mol. Opt. Phys.*, 2014, **47**, 124014.
30 U. Megerle, I. Pugliesi, C. Schriever, C. F. Sailer and E. Riedle, *Appl. Phys. B: Lasers Opt.*, 2009, **96**, 215–231.
31 S. Schott, L. Ress, J. Hrusak, P. Nuernberger and T. Brixner, *Phys. Chem. Chem. Phys.*, 2016, **18**, 33287–33302.
32 J. J. Snellenburg, S. P. Laptenok, R. Seger, K. M. Mullen and I. H. M. van Stokkum, *J. Stat. Softw.*, 2012, **49**, 1–22.
33 TURBOMOLE V7.1 2016 and V7.2.1 2017, a development of University of Karlsruhe and Forschungszentrum Karlsruhe GmbH, 1989–2007, TURBOMOLE GmbH, since 2007; available from http://www.turbomole.com.
34 A. D. Becke, *J. Chem. Phys.*, 1993, **98**, 5648–5652.

Published on 25 October 2018. Downloaded by Ruhr Universitat Bochum on 12/22/2018 1:37:31 PM.

35 S. Grimme, J. Antony, S. Ehrlich and H. Krieg, *J. Chem. Phys.*, 2010, **132**, 154104.
36 S. Grimme, S. Ehrlich and L. Georigk, *J. Comput. Chem.*, 2011, **32**, 1456.
37 F. Weigend and R. Ahlrichs, *Phys. Chem. Chem. Phys.*, 2005, **7**, 3297.
38 F. Weigend, M. Häser, H. Patzelt and R. Ahlrichs, *Chem. Phys. Lett.*, 1998, **294**, 143.
39 A. Klamt and G. Schüürmann, *J. Chem. Soc., Perkin Trans. 2*, 1993, 386.
40 B. Lunkenheimer and A. Köhn, *J. Chem. Theory Comput.*, 2013, **9**, 977.
41 J. Schirmer, *Phys. Rev. A: At., Mol., Opt. Phys.*, 1981, **26**, 2395–2416.
42 C. Hättig, *Adv. Quantum Chem.*, 2005, **50**, 37–60.
43 C. Hättig and F. Weigend, *J. Chem. Phys.*, 2000, **113**, 5154–5161.
44 N. O. C. Winter, N. K. Graf, S. Leutwyler and C. Hattig, *Phys. Chem. Chem. Phys.*, 2013, **15**, 6623–6630.
45 K. Fukui, *Acc. Chem. Res.*, 1981, **14**, 363.
46 P. Plessow, *J. Chem. Theory Comput.*, 2013, **9**, 1305–1310.
47 M. Pabst and A. Köhn, *J. Chem. Phys.*, 2008, **129**, 214101.
48 A. F. Thünemann, D. Schütt, R. Sachse, H. Schlaad and H. Möhwald, *Langmuir*, 2006, **22**, 2323.
49 R. Mundt, C. T. Ziegenbein, S. Fröbel, O. Weingart and P. Gilch, *J. Phys. Chem. B*, 2016, **120**, 9376–9386.
50 A. J. Reuss, C. Grünewald, M. Braun, J. W. Engels and J. Wachtveitl, *ChemPhysChem*, 2016, **17**, 1369–1376.
51 H. Marciniak and S. Lochbrunner, *Chem. Phys. Lett.*, 2014, **609**, 184–188.
52 C. Consani, M. Berberich, F. Würthner and T. Brixner, *Chem. Phys. Lett.*, 2017, **683**, 83–90.
53 T. Bolze, J.-L. Wree, F. Kanal, D. Schleier and P. Nuernberger, *ChemPhysChem*, 2015, **19**, 138–147.
54 S. K. Pal, J. Peon, B. Bagchi and A. H. Zewail, *J. Phys. Chem. B*, 2002, **106**, 12376–12395.
55 P. van der Meulen, H. Zhang, A. M. Jonkman and M. Glasbeek, *J. Phys. Chem.*, 1996, **100**, 5367–5373.
56 R. Adhikary, P. Mukherjee, T. W. Kee and J. W. Petrich, *J. Phys. Chem. B*, 2009, **113**, 5255–5261.
57 I. Delfino, C. Manzoni, K. Sato, C. Dennison, G. Cerullo and S. Cannistraro, *J. Phys. Chem.*, 2006, **110**, 17252–17259.
58 J.-M. L. Pecourt, J. Peon and B. Kohler, *J. Am. Chem. Soc.*, 2001, **123**, 10370–10378.
59 J. Grilj, P. Buchgraber and E. Vauthey, *J. Phys. Chem. A*, 2012, **116**, 7516–7522.
60 J. Grilj, C. Zonca, a. M. L. Daku and E. Vauthey, *Phys. Chem. Chem. Phys.*, 2012, **14**, 6352–6358.
61 F. Renth, M. Foca, A. Petter and F. Temps, *Chem. Phys. Lett.*, 2006, **428**, 62–67.
62 D. M. Carey and G. M. Korenowski, *J. Chem. Phys.*, 1998, **108**, 2669–2675.
63 W. Sawodny, K. Niedenzu and J. W. Dawson, *Spectrochim. Acta, Part A*, 1967, **28**, 799–806.
64 E. Pines, D. Huppert and N. Agmon, *J. Chem. Phys.*, 1988, **88**, 5620–5630.
65 S. A. Kovalenko, R. Schanz, H. Hennig and N. P. Ernsting, *J. Chem. Phys.*, 2001, **115**, 3256–3273.
66 M. T. Pereira, J. M. Silva-Alves, A. Martins-Jose, J. C. D. Lopes and M. M. Santoro, *Braz. J. Med. Biol. Res.*, 2005, **38**, 1593–1601.
67 N. P. Ernsting, S. A. Kovalenko, T. Senyushkina, J. Saam and V. Farztdinov, *J. Phys. Chem. A*, 2001, **105**, 3443–3453.
68 R. Ghosh and D. K. Palit, *Photochem. Photobiol. Sci.*, 2013, **12**, 987–995.
69 P. K. Verma, F. Koch, A. Steinbacher, P. Nuernberger and T. Brixner, *J. Am. Chem. Soc.*, 2014, **136**, 14981–14989.
70 T. N. V. Karsili, B. Marchetti, M. N. R. Ashfold and W. Domcke, *J. Phys. Chem. A*, 2014, **118**, 11999–12010.
71 O. F. Mohammed, D. Xiao, V. S. Batista and E. T. J. Nibbering, *J. Phys. Chem. A*, 2014, **118**, 3090–3099.
72 P. K. Verma, A. Steinbacher, F. Koch, P. Nuernberger and T. Brixner, *Phys. Chem. Chem. Phys.*, 2015, **17**, 8459–8466.
73 P. K. Verma, A. Steinbacher, A. Schmiedel, P. Nuernberger and T. Brixner, *Struct. Dyn.*, 2016, **3**, 023606.
74 J. J. Szymczak, M. Barbatti and H. Lischka, *J. Phys. Chem. A*, 2009, **113**, 11907–11918.
75 P. Plessow, *J. Chem. Theory Comput.*, 2013, **9**, 1305–1310.